Texas A&M University
Mechanical Engineering Department
Turbomachinery Laboratory
Tribology Group

AN IMPROVED BULK-FLOW ANALYSIS FOR INTERLOCKING LABYRINTH GAS SEALS: LEAKAGE AND FORCE COEFFICIENTS

TRC-SEAL-02-17

Research Progress Report to the Turbomachinery Research Consortium
by

Luis San Andrés
Mast-Childs Chair Professor
Principal Investigator

Tingcheng Wu
Research Assistant

May 2017

PRESSING NEEDS FOR SEALS /BEARING SOFTWARE DEVELOPMENT/UPDATE
TRC Project, TEES # 400124-00027

EXECUTIVE SUMMARY

Gas labyrinth seals (LS) restrict secondary flows (leakage) in turbomachinery. Their impact on the efficiency and rotordynamic stability of high pressure compressors and steam turbines can hardly be overstated. Hence, the capability to (quickly and) accurately predict LS leakage and rotordynamic force coefficients is crucial to assess their impact on turbomachine design, operation and troubleshooting.

This report details updates to the BFM program XLLABY© to predict the leakage and the rotordynamic force coefficients for interlocking labyrinth seals (LS) and stepped LSs. The BFM is based on the 1980' one-control volume model of Childs and Scharrer. The current analysis focuses on the flow conditions leading to a choked flow and presents a simple equation to estimate its appearance.

Predictions of leakage and cavity pressures for an ILS correlate well with 2D CFD flow predictions, even for a choked flow operating condition. Current BFM predictions for force coefficients are compared against test data published in 1995 by Childs and students. The correlation is good for cross-coupled stiffness and direct damping, in particular. Direct stiffness; albeit small, does not agree with the test results. A last example uses a test stepped LS and predictions of leakage are in agreement with measured magnitudes.

The revamped XLLABY© graphical user interfaces presently offers options for LSs with teeth on rotor, teeth of stator, and an interlocking labyrinth seal. The seal configuration is quickly tailored by the program user without effort.

TABLE OF CONTENTS

LIST OF FIGURES

LIST OF TABLES

1. INTRODUCTION

Commonly found in gas and steam turbines and compressors, labyrinth seals (LS) control the leakage (secondary flow) from a high pressure region to a low pressure region. A typical LS comprises of cavities and teeth facing a spinning rotor. The tortuous gas flow through the cavities induces a pressure drop to control the leakage. A see-through LS has all the teeth either on the rotor (TOR) or on the stator (TOS), while an interlocking design (ILS) has teeth on the rotor as well as on the stator. LS leakage depends on seal geometry (tooth shape, pitch/depth, and number of cavities), gas type, and the operating shaft speed, pressure and temperature (inlet and outlet).

During operation, seals not just restrict a secondary flow but also produce reaction forces acting on the rotor. These forces may introduce rotordynamic instability to a rotating system, as reported in Ref. [1, 2] for example. Therefore, the capability to accurately predict LS leakage and rotordynamic force coefficients is crucial for the efficient and rotordynamic stable operation of turbomachinery.

The force developed by a LS is typically lower than those of liquid seals. For small amplitude rotor displacements (X,Y) about its centered condition, the force components (F_X, F_Y) are modeled as

$$-\begin{bmatrix} F_X \\ F_Y \end{bmatrix} = \begin{bmatrix} K & k \\ -k & K \end{bmatrix} \begin{bmatrix} X \\ Y \end{bmatrix} + \begin{bmatrix} C & c \\ -c & C \end{bmatrix} \begin{bmatrix} \dot{X} \\ \dot{Y} \end{bmatrix} \tag{1}$$

where (K, C) stand for the direct stiffness and damping coefficients; and (k, c) for the cross-coupled stiffness and damping, respectively. In a gas seal the force coefficients are functions of the excitation frequency (ω). LSs because of the working gas small density[1] offer negligible added mass terms.

The literature is abundant on detailing experimental results and models for LS leakage and rotordynamic coefficients [2]. Most research focuses on "see-through" LSs, that is seals with a uniform clearance and all the teeth on either the stator (TOS), see Figure 1 (a), or all on the rotor (TOR), see Figure 1(b).

[1] This assertion is not valid for seals handing sCO_2 at high pressures, for example

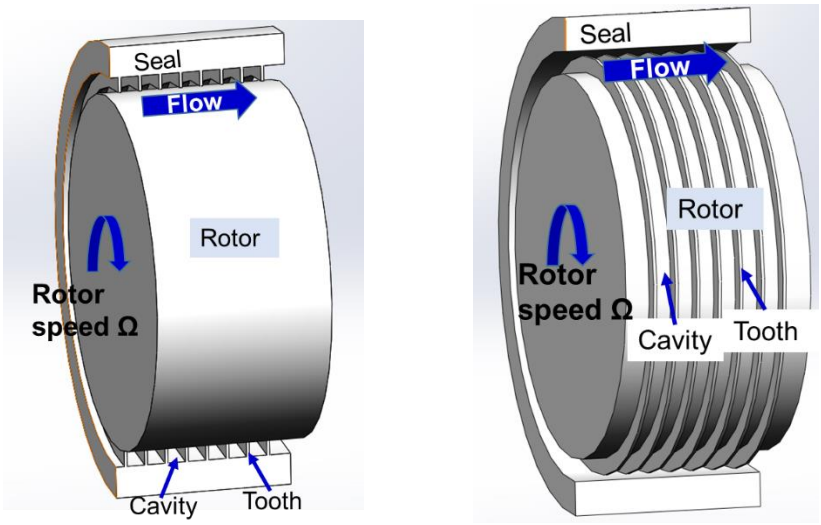

(a) **(b)**

Figure 1. See through labyrinth gas seal: (a) teeth on stator (TOS), (b) teeth on rotor (TOR).

The interlocking labyrinth seal (ILS) configuration, as shown in

Figure 2, increases the overall flow resistance as the gas passes through a narrow clearance. Therefore, the ILS relatively leaks less compared to conventional TOS and TOR LS designs. As shown in

Figure 3, the flow moves through a tortuous path and displays two regimes; namely a core flow and recirculation zones in the cavities. The core flow is a jet through flow in the leakage path which plays a dominant role in determining seal leakage. The recirculation zones in a cavity contribute to mechanical energy dissipation.

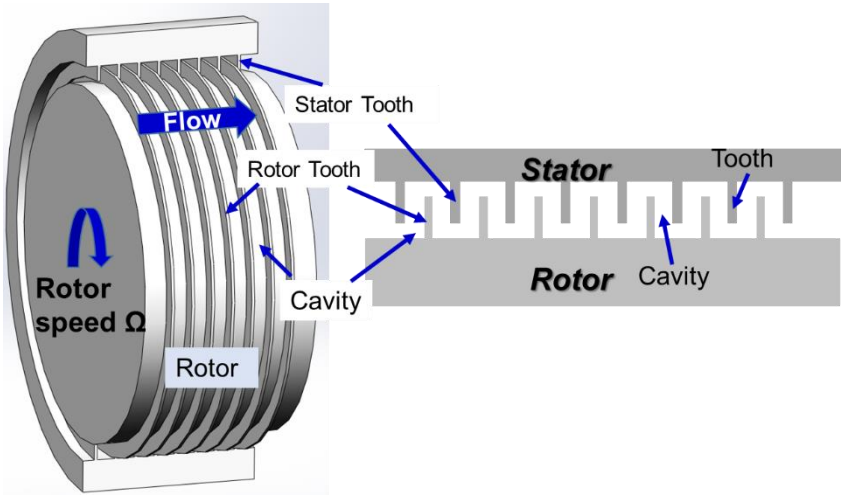

Figure 2. Interlocking labyrinth gas seal.

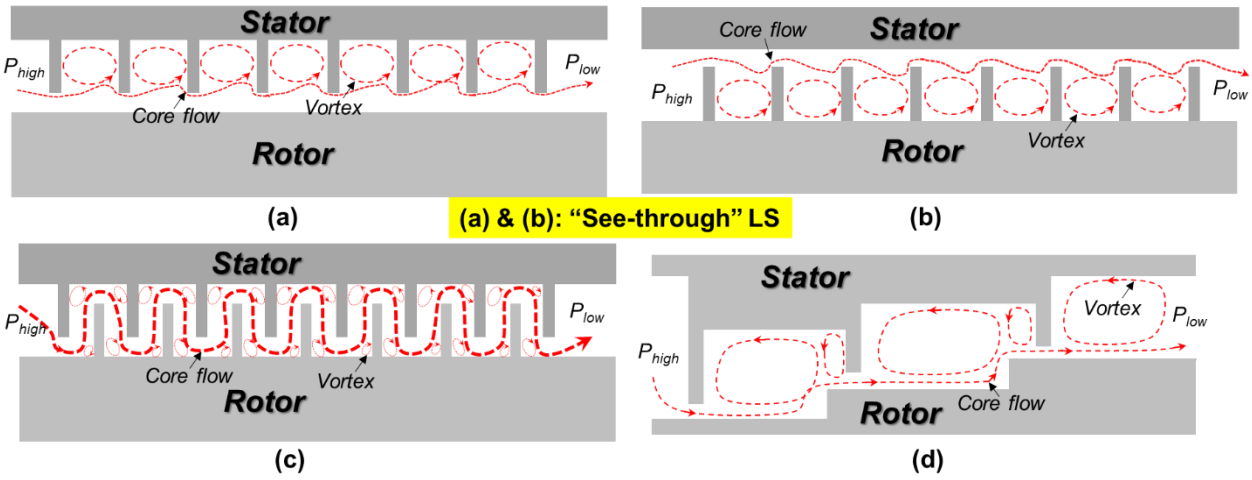

Figure 3. Schematic views of flow passing through the clearance channel in a seal: (a) TOS, (b) TOR, (c) ILS, (d) stepped LS [3].

Recently, using a CFD approach, Kuwamura et al. [3] developed a new high-performance labyrinth seal, see

Figure 4. This improved LS design reduces leakage up to 30% when compared to conventional *see-through* labyrinth seals.

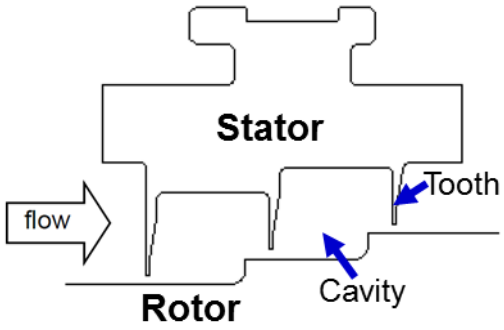

Figure 4. Improved (stepped)labyrinth gas seal [3].

A modern compressor balance drum usually employs an interlocking labyrinth seal (ILS) to hold a higher pressure drop, and thus this seal has a significant influence on rotor stability [4]. However, scant results for interlocking or the stepped labyrinth seals are available.

This report presents an improved bulk-flow model (BFM) to predict the leakage and rotordynamic force coefficients for interlocking and stepped labyrinth seals. The model predictions are compared against ILS test data available in Elrod et al. [5].

2. LITERATURE REVIEW

In 1978, Benckert and Wachter [6] measure the stiffness of labyrinth seals (TOS, ILS, and stepped LS) and investigate the influence of rotor speed and circumferential pre-swirl velocity on seal reaction forces. Their results show that the reaction forces are sensitive to the inlet flow pre-swirl, whereas the influence of rotor speed is minor for a seal with small number of teeth (less than 5). "Swirl webs", a first instance of swirl brakes, could sufficiently reduce the inlet pre-swirl velocity, and accordingly the seal destabilizing forces. Test rotordynamic force coefficients remain approximately constant and are independent of rotor eccentricity to 50% of the seal clearance. The test results support the "eccentricity independent" model discussed in Ref. [2]. Benckert and Wachter find no appreciable difference in the cross-coupled stiffness of an ILS and a TOS LS. Measured stiffness coefficients for a comparatively long ($L/D \rightarrow 1$) LS are negative. Later in 1984, Leong and Brown [7] (1984) report similar results, i.e., most TOR and TOS LSs show a negative direct stiffness; exception is noted for a short LS ($L/D = 0.1$) with only five cavities that produced a positive stiffness.

In 1986, Childs and Scharrer [8] test TOR & TOS labyrinth seals and report their rotordynamic force coefficients. The authors present direct damping coefficients for the first time. The test results show the stiffness and damping coefficients are sensitive to the inlet tangential (swirl) velocity and increase with an increase in inlet pressure. Later, Thieleke and Stetter (1990) [9] point out that the cross-coupled force, arising within each cavity, depends on the change of circumferential velocity from one cavity to the next.

In 1988, Childs et al. [10] measured the leakage and force coefficients for an ILS (C_r = 0.25 mm, average tooth pitch is 5 mm, $L/D = 0.34$) and a TOS LS (C_r = 0.305 mm, tooth pitch is 4 mm, $L/D = 0.30$). The authors test the seals at a rotor speed up to 16,000 rpm ($\frac{1}{2}D\Omega$ = 126 m/s) while the supply pressure ranges from 3.0 bar to 8.0 bar ($PR = P_{in}/P_{out}$ = 3.0-8.0). The test results evidence the ILS leaks substantially less (up to 60%) than the conventional TOS LS. Childs notes the ILS has frequency dependent rotordynamic force coefficients, which in the 1980s posed a conflict with the generally-held view that force coefficients provide a frequency-independent relation between reaction forces and rotor displacements. Compared to see-through (TOR and TOS) Ls designs, the ILS usually has a lower and negative cross-coupled stiffness (k). However, a see-through LS shows approximately twice the direct damping coefficient than the corresponding coefficient in an ILS. The direct stiffness coefficient (K) for both configurations is negative; the see-through configuration shows half the magnitude of the direct stiffness for the ILS.

Further test results from Picardo and Childs (2005) [11], Wagner et al. (2009) [12], Ertas et al. (2012) [13] and Vannini et al. (2014) [14] show that LSs possess strongly frequency dependent rotordynamic force coefficients; in particular, the direct stiffness and effective damping coefficients. The test cross-coupled

stiffness is only sensitive to the inlet pre-swirl velocity and not rotor speed. Thus, inlet pre-swirl has a stronger influence on the effective damping than rotor speed.

Besides the experimental investigations, theoretical analyses for labyrinth seals are well documented. Since Alford [15] published in 1965 an analysis of the destabilizing forces caused by labyrinth seals, researchers have produced analyses predicting the leakage and rotordynamic force coefficients of labyrinth seals. Notable to this day are the bulk-flow models (BFM) advanced by Vance and Murphy [16], Kostyuk [17], Iwatsubo et al. [18, 19], and Childs and Scharrer [20].

Later, in 1988, Scharrer [21] introduces a two-control volume (CV) BFM that accounts for the vortex in a cavity. Along the dividing streamline, the interface between the two control volumes, a 2D jet flow model accurately predicts the recirculation velocity. Compared to test results, Scharrer's model accurately predicts cross-coupled stiffness (k) for both TOR and TOS LSs and shows an improvement in the prediction of direct damping coefficient (C) [22].

As commercial software is readily accessible and computers processing speed continuously increase, computational fluid dynamics (CFD) analysis based approaches to solving the Navier-Stokes equations of turbulent flow in seals is (becoming) common engineering practice. Moore [23] and Li et al. [24] report CFD derived LS predictions showing good correlation to experimental data for both rotordynamic force coefficients and leakage. The authors claim a (marginal) improvement over BFM predictions.

Unlike bulk-flow techniques, CFD makes no assumptions on the geometry, thus allowing (with a few million nodes) the analysis of flow in an arbitrarily shaped domain, including stepped LSs and ILSs. In 2013, Gao and Kirk [4] numerically investigated an ILSs with a commercial CFD software and applied a rotating frame transformation to convert the transient state flow (with a whirling rotor) to a steady state one. The authors assume the rotordynamic force coefficients are frequency independent. Unfortunately, prior test results [10] show the rotordynamic force coefficients of the ILs are frequency dependent. Therefore, the obtained CFD predictions may need further validation.

CFD simulations are still time consuming and computationally expensive. Migliorini et al. [25, 26] present a new CFD/Bulk-flow hybrid method to determine rotordynamic coefficients of gas seals. Briefly, the authors utilize CFD to determine the steady state bulk-flow variables (pressure, and averaged velocities across the clearance), and a bulk-flow perturbation method to obtain the reaction forces of an eccentric whirling rotor. This hybrid method predictions shows better accuracy with experimental results in Ref. [27], as compared to a conventional BFM. With a computation time on the order of a typical bulk-flow analysis, the CFD/BFM hybrid method predicts rotordynamic characteristics comparable to the full 3D transient CFD analysis.

In 2016, the Turbomachinery Research Consortium (TRC) funded a project to update the available BFM for LS and to integrate a capability to model interlocking LSs. This report presents an update to the BFM program (XLLABY©) and a comparison of its predictions against archival test data.

3. GOVERNING EQUATIONS

In 1986, Childs and Scharrer [20] (based on Iwatsubo's model [18, 19]) derived the equations of a one control volume bulk flow model for a labyrinth seal. The following update follows the same method.

Figure 5 shows schematic views of an ILS with radial clearance C_r and rotor radius R_s. Teeth on both the rotor and the stator have the same geometry, with B as a tooth height and L_i as a tooth pitch.

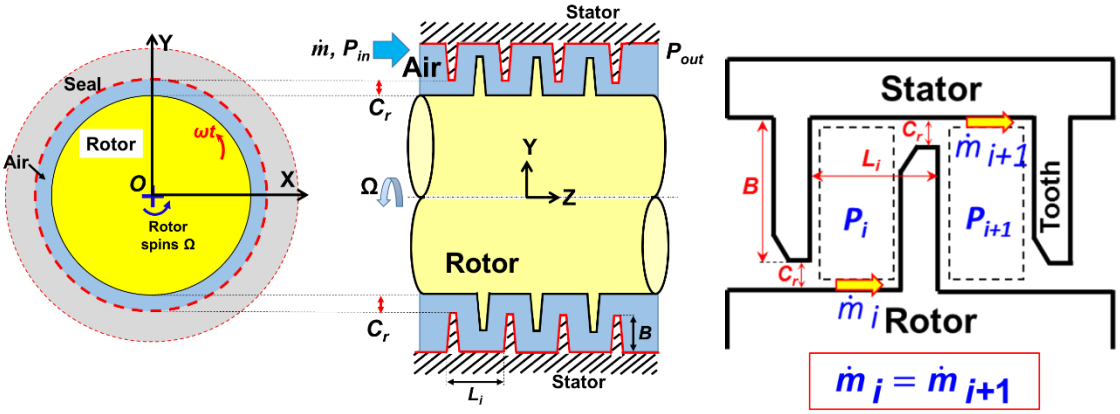

Figure 5. Schematic views (not to scale) of an interlocking labyrinth seal (ILS) and an one-control-volume model

The flow domain is divided into n cavities separated by blades. Within the i^{th} cavity, the pressure is P_i and the mean circumferential velocity is U_i. The velocity U_i differs from one cavity to the next, but it is sufficiently similar in a single cavity to permit its bulk flow representation. The mass flow rate through the upstream and downstream teeth $\dot{m}_i=\dot{m}_{i+1}$. The gas density (ρ_i) follows the ideal gas law, $\rho_i=P_i/(Z_gR_gT)$, where R_g and Z_g are the gas constant and the gas compressibility factor, and T is the gas temperature[2].

In the i^{th} cavity, the flow mass conservation equation and momentum transport equation along the θ direction are [20]:

$$\frac{\partial(\rho_i A_i)}{\partial t}+\frac{\partial(\rho_i U_i A_i)}{R_s\,\partial\theta}+\bar{\dot{m}}_{i+1}-\bar{\dot{m}}_i=0 \tag{2}$$

$$\frac{\partial(\rho_i U_i A_i)}{\partial t}+\frac{\partial(\rho_i A_i U_i^{\,2})}{R_s\,\partial\theta}=-\frac{A_i}{R_s}\frac{\partial P_i}{\partial\theta}+(\tau_{r_i}a_{r_i}-\tau_{s_i}a_{s_i})L_i \tag{3}$$

[2] The model assumes isothermal flow conditions.

$$\dot{m}_i = \pi D \bar{\dot{m}}_i = \mu_{1i}\mu_{2i}\left(\pi D C_r\right)\sqrt{\frac{P_{i-1}^2 - P_i^2}{R_g T}} \tag{4}$$

Above $A_i = (B + C_r)L_i$ is the area of a cavity cross-section. Eq. (4) is the well-known Neumann's equation [2] that relates the mass flow rate $\dot{m}$ through a teeth as a function of the difference in upstream and downstream cavity pressures, P_{i-1} and P_i . $\bar{\dot{m}}$ is the mass flow rate per circumference length. In Eq. (4), μ_{1i} is the kinetic energy carry-over coefficient, and μ_{2i} is a flow discharge coefficient (see later equations).

In Eq. (3) a_{r_i} and a_{s_i} are dimensionless lengths introduced in Ref. [2]. For **TOR LS**: $a_{r_i} = (2B + L_i)/L_i,\ a_{s_i} = 1$; **TOS LS**: $a_{r_i} = 1,\ a_{s_i} = (2B + L_i)/L_i$. Since the ILS has teeth both on stator and rotor, $a_{r_i} = a_{s_i} = (B + L_i)/L_i$.

The shear stress (τ_{r_i}, τ_{s_i}) acting on the rotor and stator are defined in terms of friction factors (f_r, f_s) [2]:

At the rotor surface:
$$\tau_{r_i} = f_{r_i}\left(\frac{1}{2}\rho_i U_{r_i}^2\right) = n_r\,\mathrm{Re}_r^{m_r}\left(\frac{1}{2}\rho_i U_{r_i}^2\right) \tag{5}$$

where
$$\mathrm{Re}_r = \frac{\left|R_s\Omega - U_i\right| D_{h_i}}{\nu_i},\ U_{ri} = R_s\Omega - U_i$$

At the stator surface
$$\tau_{s_i} = f_{s_i}\left(\frac{1}{2}\rho_i U_{s_i}^2\right) = n_s Re_s^{m_s}\left(\frac{1}{2}\rho_i U_{s_i}^2\right) \tag{6}$$

where
$$Re_s = \frac{\left|U_i\right| D_{h_i}}{\nu_i},\ U_{s_i} = U_i$$

Above n_r, m_r, n_s and m_s are empirical coefficients (usually for a smooth surface, $n_r = n_s = 0.079$, $m_r = m_s = -0.25$) [2], and D_{h_i} is the hydraulic diameter

$$D_{h_i} = \frac{2(C_r + B)L_i}{(C_r + B + L_i)} \tag{7}$$

Following Childs and Scharrer [20], subtracting Eqn.(2) times U_i from Eqn.(3) yields the following primitive form of the momentum Eqn. (3):

$$\rho_i A_i \frac{\partial U_i}{\partial t} + \rho_i U_i A_i \frac{\partial U_i}{R_s \partial \theta} + \bar{\dot{m}}_i (U_i - U_{i-1}) = -\frac{A_i}{R_s}\frac{\partial P_i}{\partial \theta} + (\tau_{r_i} a_{r_i} - \tau_{s_i} a_{s_i})L_i \tag{8}$$

At the seal inlet and exit planes, the pressure undergoes a pressure drop and rise due to fluid inertia. Let $W = (\dot{m}/\rho)/(\pi D C_r)$ be a bulk-flow axial velocity. Then

$$P_i = P\big|_{z=0} = P_{in} + \frac{\rho}{2}(1+\xi)W^2\Big|_{z=0},\quad \xi = 0 \tag{9}$$

$$P_i = P\big|_{z=L} = P_{out} + \frac{\rho}{2} C_s W^2\Big|_{z=L}, \quad C_s = 0 \tag{10}$$

where ξ is an entrance loss coefficient, and C_s is an exit pressure recovery coefficient. In addition, the entrance circumferential velocity into the seal is $U\big|_{z=0} = \alpha R\Omega$, with α as a known inlet pre-swirl ratio.

Perturbation Analysis. For the i^{th} cavity, the continuity equation (2), circumferential momentum equation (3) and leakage equation (4) are the governing equations for the variables U_i, P_i, and m_i. For small amplitude rotor motions ($\Delta e_x, \Delta e_y$) of frequency ω, the film thickness (H) is given by the real part of

$$H = H_0 + e^{j\omega t}(\Delta e_x \cos\theta + \Delta e_y \sin\theta), \quad H_0 = C_r \tag{11}$$

The velocity, and pressure fields are expressed as the sum of a zeroth order and first order complex fields, describing the equilibrium condition and the perturbed motions, i.e.

$$\phi = \phi_0 + e^{jwt}(\Delta e_x \phi_x + \Delta e_y \phi_y) \tag{12}$$

with $\phi = \{P, U, \ldots\}$.

Substitution of the flow variables into the governing equations yields the differential equations for the zeroth and first order flow fields.

The zeroth order equations are simply

$$\bar{\dot{m}}_i = \bar{\dot{m}}_{i+1} \tag{13}$$

$$\bar{\dot{m}}_0 (U_{0i} - U_{0i-1}) = (\tau_{r0i} a_{r_i} - \tau_{s0i} a_{s_i}) L_i \tag{14}$$

To determine the mass flow rate $\dot{m}_0$, the cavity pressures $(P_i)_0$ and the velocity field $(U_i)_0$ for a rotor centered position. First-order equations are not detailed for brevity.

San Andrés [28] details the finite volume method implemented to solve the nonlinear partial differential equations governing the flow. The perturbation analysis renders the seal static and dynamic reaction forces as

$$-\begin{bmatrix} F_{X(\omega)} \\ F_{Y(\omega)} \end{bmatrix} = -\begin{bmatrix} F_{X0} \\ F_{Y0} \end{bmatrix} + \begin{bmatrix} D_{(\omega)} & E_{(\omega)} \\ G_{(\omega)} & F_{(\omega)} \end{bmatrix} \begin{bmatrix} X_{(\omega)} \\ Y_{(\omega)} \end{bmatrix} \tag{15}$$

The functions *D*-*F* are frequency-dependent and obtained as

$$\begin{bmatrix} D \\ G \end{bmatrix}_{(\omega)} = R_s \int_0^L \int_0^{2\pi} P_X \begin{bmatrix} \cos\theta \\ \sin\theta \end{bmatrix} d\theta\, dz; \quad \begin{bmatrix} E \\ F \end{bmatrix}_{(\omega)} = R_s \int_0^L \int_0^{2\pi} P_Y \begin{bmatrix} \cos\theta \\ \sin\theta \end{bmatrix} d\theta\, dz \tag{16}$$

Note that for concentric rotor position, $D = F(j\omega)$, $E = -G$. Stiffness and damping coefficients follow from

$$K_{(\omega)} + j\,\omega C_{(\omega)} \leftarrow D_{(\omega)}; \; k_{(\omega)} + j\,\omega c_{(\omega)} \leftarrow D_{(\omega)} \tag{17}$$

The BFM analysis procedure is well documented in Refs. [2, 20, 28]. In brief, the BFM solution procedure follows the steps:

(1) Determine whether the flow is choked or not by comparing the inlet pressure against the critical inlet pressure (as discussed later);

(2) Calculate the mass flow rate, cavity pressure distribution and the cavity circumferential velocity.

(3) Solve the first order (perturbed) equations for a given whirl frequency (ω), integrate the dynamic pressure acting on the rotor surface to calculate the reaction forces, and thus obtaining the rotordynamic force coefficients.

4. LEAKAGE, PRESSURE DISTRIBUTION AND CIRCUMFERENTIAL VELOCITY IN AN INTERLOCKING LABYRINTH SEAL

For a LS gas flow that is unchoked, the ratio of inlet (supply) pressure (P_{in}) and outlet (discharge) pressure (P_{out}) must satisfy [29]:

$$\frac{P_{in}}{P_{out}} < r_c = \left(\frac{\gamma+1}{2}\right)^{\frac{\gamma}{\gamma-1}} \sqrt{b_1 \mu_1^{\,2} + b_1 (NT-2) + 1} \quad (=4.4, \text{ for ILS listed in Table 1}) \tag{18}$$

where, $b_1 = 1 - \left(\frac{\gamma+1}{2}\right)^{-\frac{2\gamma}{\gamma-1}}$ (=0.729, for air). Thus, in the BFM, the first step checks whether the flow is choked or not through Eqn. (18). Note the critical pressure ratio (r_c) is a function of the number of teeth (NT). Increasing the number of teeth raises r_c.

For a *see-through* labyrinth seal (TOR or TOS) with diameter D, the Neumann's empirical leakage equation (Eqn. (4)) with Chaplygin's [30] flow coefficient (μ_{2i}) predicts the gas leakage ($\dot{m}$) across a seal tooth with tip clearance C_r [2, 29]. For a *see-through* (TOR a TOS) labyrinth seal, the kinetic energy carry-over coefficient (μ_{1i}) is a function of the seal geometry

$$\lambda = 1 - \left(1 + 16.6\, C_r / L_i\right)^{-2} \tag{19}$$

$$\mu_{1i} = \left(\frac{NT}{(1-\lambda)\, NT + \lambda}\right)^{\frac{1}{2}} \tag{20}$$

For the first tooth in a see-through LS and all the teeth in an ILS, μ_{1i} equals unity [2]. Note λ is constant in a seal with uniform teeth spacing (cavity widths and depth). For a typical 7 teeth ILS (C_r = 0.2 mm, L_i = 5 mm), C_r/L_i = 0.04; thus $\lambda \sim 0.64$.

Table 1 lists the geometry and operating conditions of an ILS with four teeth on the stator and three teeth on the rotor surface (NT=7). The first tooth (facing a high pressure) is on the stator. Figure 6 depicts an axial view of the seal (ILS) with lengthy upstream and downstream sections considered for a CFD

analysis. Childs [2] recommends a kinetic energy carry-over coefficient (μ_{1i}) = 1 for use in the leakage Eqn. (4) across all teeth of an interlocking seal.

Table 1. Interlocking labyrinth seal dimensions (4 teeth on stator and 3 teeth on rotor[3]), gas properties and operating conditions.

Seal Geometry	Overall length, L	41.79 mm
	Inner diameter, D	150 mm
	Radial clearance, C_r	0.2 mm
	Teeth number, NT	7
	Tooth pitch, L_i	3.75 mm
	Height, B	3 mm
	Width at tip, L_t	0.3 mm
Gas Properties	Density(at 12 bar), ρ	13.9 kg/m^3
	Kinematic viscosity, v	1.51×10^{-5} m^2/s
	Temperature, T	300 K
Operating Conditions	Supply pressure, P_{in}	13 bar
	Discharge pressure, P_{out}	5 bar
	Pressure Ratio, $PR = P_{in}/P_{out}$	2.6
	Rotor speed, Ω	7,500 rpm ($\frac{1}{2}D\Omega \approx 59$ m/s)
	Inlet Pre-swirl Ratio, α	0

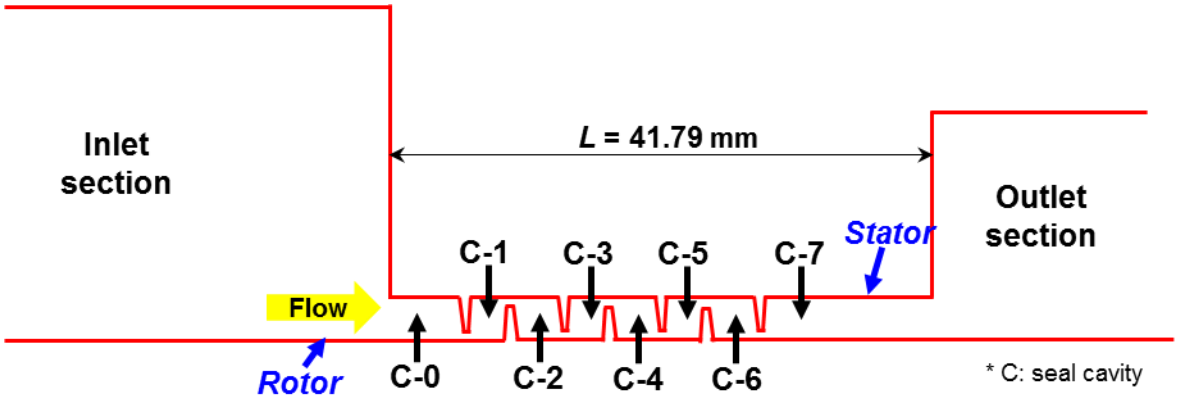

Figure 6. Schematic view of an interlocking labyrinth seal, C-: cavity number. 4 teeth on stator and 3 on rotor (*NT*=7).

The flow discharge coefficient μ_{2i} uses Chaplygin's formula, Gurevich (1966) [2, 29] as

$$\mu_{2i} = \frac{\pi}{\pi + 2 - 5\beta_i + 2\beta_i^2} \tag{21}$$

with

$$\beta_i = \left(\frac{P_{i-1}}{P_i}\right)^{\frac{\gamma-1}{\gamma}} - 1 \tag{22}$$

where γ is the ratio of specific heats. For air, γ=1.4. Let, as in Ref. [29],

[3] ILS being tested at TAMU in 2017.

$$\dot{m} = \frac{\dot{m}\sqrt{R_g T}}{\pi D C_r} \tag{23}$$

Since $\dot{m} = \dot{m}_1 = \dot{m}_2 = \cdots = \dot{m}_{NT}$, and using Eqn. (4), let

$$k_1 = \frac{\dot{m}}{\mu_{2i}} = \mu_{1i}\sqrt{P_{i-1}^2 - P_i^2} \tag{24}$$

Thus, for i=1, μ_{1i}=1,

$$P_0^2 - P_1^2 = k_1^2 \tag{25}$$

Since all teeth and cavities are equal, then

$$P_1^2 - P_2^2 = \frac{k_1^2}{\mu_{1*}^2}; \quad P_2^2 - P_3^2 = \frac{k_1^2}{\mu_{1*}^2}; \quad ....; P_6^2 - P_7^2 = \frac{k_1^2}{\mu_{1*}^2} \tag{26}$$

Recall $\mu_{12} \ldots = \mu_{17} = \mu_{1*} = 1$. Add Eqns. (27) and (28) to obtain

$$k_1 = \sqrt{\frac{P_0^2 - P_{NT}^2}{1 + \frac{(NT-1)}{\mu_{1*}^2}}} \tag{27}$$

with $P_0 = P_{in} = 1.3\times10^6$ Pa, $P_7 = P_{out} = 5\times10^5$ Pa; Eqn. (29) delivers k_1=6.6×10^5 Pa. The gas pressure at the first cavity follows from Eqn. (24) as $P_1^2 = k^2 - P_0^2$. Pressures in the subsequent cavities use Eqn. (26). Next, a β_i coefficient, Eqn. (22), is calculated from the ratio $\left(P_{i-1}/P_i\right)$, and Eqn. (21) delivers the flow discharge coefficient μ_{2i}. Recall that mass flow continuity implies $\dot{m}_1 = \dot{m}_2 = \cdots \dot{m}_{NT} = \dot{m}$, Eqn. (4) produces the mass flow rate ($\dot{m}_i$) through each tooth.

The distribution of circumferential velocity in the seal is of importance in determining the fluid induced stresses on the shaft. Solving Eqn. (3) with the cavity pressures and mass flow rate obtained delivers the bulk-flow circumferential velocity (U_i) in each cavity.

In a (separate) 2D CFD (adiabatic) flow study, the interlocking labyrinth seal (ILS) operates with an ideal gas (T_{in}= 300 K) with zero pre-swirl (well upstream of the inlet plane). Table 1 lists the seal geometry and operating conditions. Table 2 lists the mass flow rate ($\dot{m}_i$) predictions and cavity pressures (P_i) using Neumann's leakage model with $\mu_{1i=1,2..7}$ = 1. The predicted mass flow rate $\dot{m}$ = 96 g/s is 8% lower than the CFD flow analysis prediction ($\dot{m}_{CFD}$ =105 g/s).

Figure 7 plots the cavity pressure (P_i) and the ratio (P_i/P_{in}) vs. cavity number. The predictions derived from Neumann's leakage model show good agreement with the CFD results. 2D CFD analyses of a TOS LS and a TOR LS with the same tooth geometry, rotor diameter, seal clearance and operating conditions

evidence that the ILS restricts more flow and shows a ~30% lower leakage than the TOS and TOR LSs ($\dot{m}_{TOR,\ TOS}$ = 157 g/s).

Figure 8 shows the CFD and BFM predicted average (bulk-flow) circumferential velocity (U_i) vs. the cavity number. The maximum discrepancy between the BFM and CFD predictions is ~ 8%, i.e. good agreement. The CFD analysis delivers a maximum Mach number ~ 0.8 across the last tooth, i.e. when the flow exits the seal.

Table 2. BFM predictions of flow, cavity pressures and coefficient μ_{2i} for an interlocking labyrinth seal (μ_{1i} =1). ILS with P_{in} = 13 bar, P_{out}= 5 bar, PR = 2.6, rotor speed 7,500 rpm.

	Cavity	Pressure [bar]	β_i	μ_{2i}	Leakage [g/s]
	inlet	13.0			
	1	12.1	0.02	0.62	
	2	11.1	0.02	0.63	
PR = 2.6	3	10.1	0.03	0.63	
(P_{in}/P_{out})	4	8.9	0.04	0.63	96
	5	7.6	0.05	0.64	
	6	6.1	0.07	0.65	
	outlet	5.0	0.06	0.65	

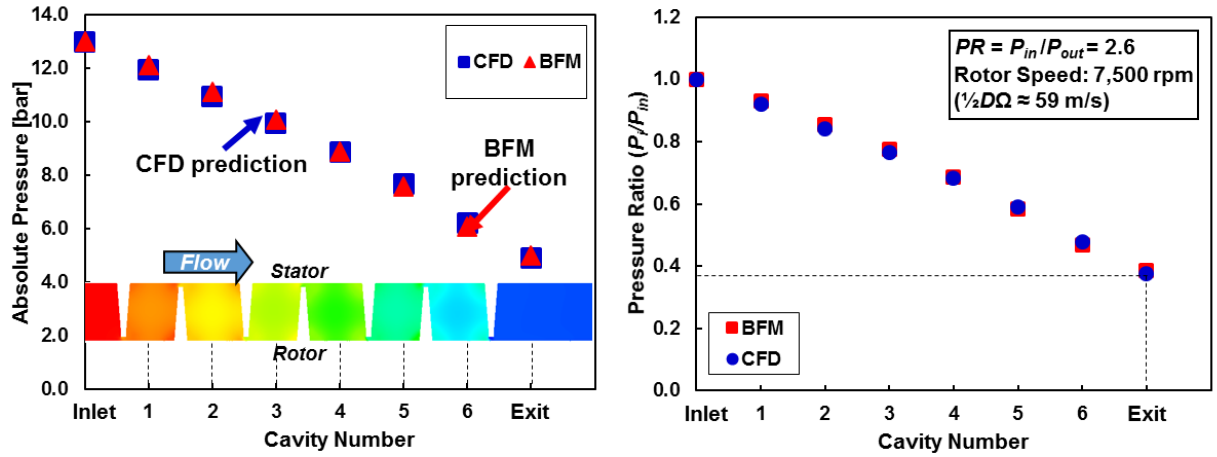

(a) **(b)**

Figure 7. CFD and BFM predictions: (a) cavity absolute pressure, (b) pressure ratio P_i/P_{in} vs. cavity. ILS (4 TOS+3 TOR). Air at T=300 K, P_{in} =13 bar, P_{out} = 5 bar, PR =P_{in}/P_{out} =2.6, and rotor speed 7,500 rpm (½$D\Omega \approx$ 59 m/s).

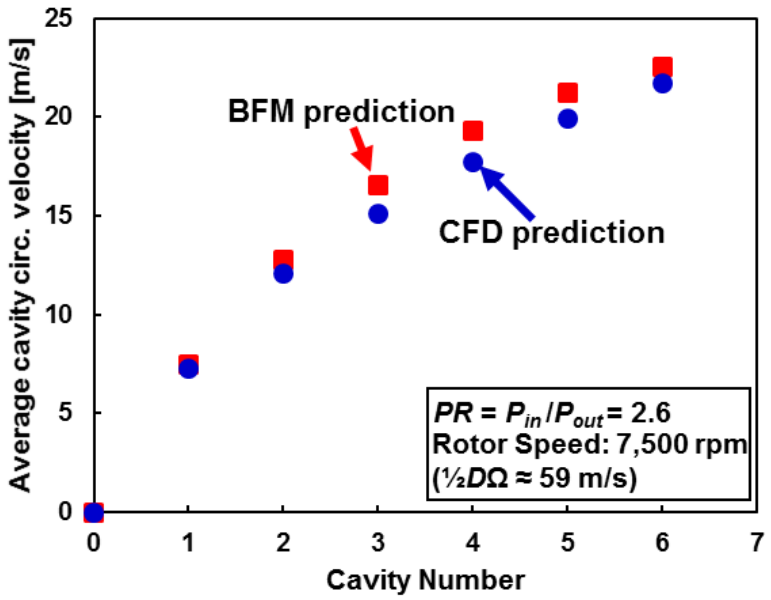

Figure 8. CFD and BFM predicted average (bulk-flow) circumferential velocity vs. cavity. ILS (4 TOS+3 TOR). Air at T=300 K, P_{in} =13 bar, P_{out} = 5 bar, PR =P_{in}/P_{out} =2.6, and rotor speed 7,500 rpm (½$D\Omega$ ≈ 59 m/s).

Choked Gas Flow Case For choked flow (i.e. whose Mach number =1), the calculation starts with a guess pressure value of the cavity before the last tooth. With the guess pressure value of (NT-1) cavity, the mass flow rate across ($\dot{m}$) the last tooth is

$$\dot{m}_{NT} = \frac{\mu_{1\_NT}\mu_{2\_NT}\left(\pi DC_r\right)P_{NT-1}}{\sqrt{R_g T}}\sqrt{1-\left(\frac{P_{NT}}{P_{NT-1}}\right)} \tag{28}$$

Recall the mass flow continuity ($\dot{m}_i=\dot{m}_{i+1}=\cdots=\dot{m}_{NT}$); thus, the upstream cavity pressures (P_i) are obtained through the steps discussed in section 3.1.

A 2D CFD analysis for the ILS in Table 1 (½$D\Omega$ ≈ 59 m/s) shows that the flow is choked when the supply pressure P_{in} = 13 bar, i.e., a pressure ratio PR = P_{in}/P_{out} = 6.5. Table 3 lists the predictions of flow rate, cavity pressures, and leakage coefficients (μ_{1i} and μ_{2i}). The BFM model under-predicts the mass flow rate by ~7%, i.e. $\dot{m}$ ~101 g/s < $\dot{m}_{CFD}$ ~109 g/s. The CFD analysis delivers a maximum Mach number ~ 1.4 across the last tooth tip.

Figure 9 graphs the predicted cavity pressures (P_i) and the pressure ratio (P_i/P_{in}) vs. the seal cavity number for the above choked flow case (P_{in} = 13 bar, PR = 6.5). The graph reveals that the predictions agree well with the CFD results.

Table 3. BFM Predictions of flow, cavity pressures and coefficient μ_{2i} for an interlocking labyrinth seal (μ_{1i} =1). ILS with P_{in} = 13 bar, P_{out}= 2 bar, rotor speed 7,500 rpm (½$D\Omega$ ≈ 59 m/s).

	Cavity	Pressure [bar]	β_i	μ_{2i}	Leakage [g/s]
PR = 6.5 (P_{in}/P_{out})	inlet	13.0			
	1	12.0	0.02	0.63	
	2	10.9	0.03	0.63	
	3	9.7	0.03	0.63	
	4	8.4	0.04	0.64	101
	5	6.8	0.06	0.65	
	6	5.0	0.10	0.67	
	outlet	2.0	0.20	0.74	

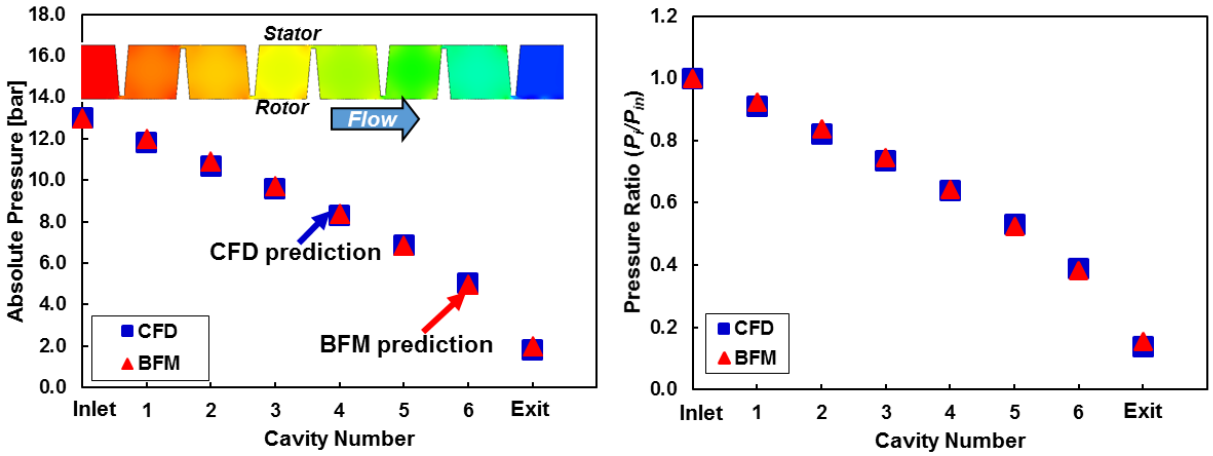

Figure 9. BFM and CFD predictions: (a) cavity absolute pressure, (b) pressure ratio P_i/P_{in} vs. cavity. ILS (4 TOS+3 TOR). Air at T=300 K, P_{in} =13 bar, P_{out} = 2 bar, PR = 6.5, and rotor speed 7,500 rpm (½$D\Omega$ ≈ 59 m/s). $\dot{m}$ = 101 g/s, $\dot{m}_{CFD}$= 109 g/s.

5. ROTORDYNAMIC FORCE COEFFICIENTS

Elrod et al. [5] report[4] experimental rotordynamic force coefficients (direct stiffness *K*, cross-coupled stiffness *k*, and direct damping *C*) for the ILS depicted in

Figure 10. Table 4 lists the seal geometry and operating conditions. The seal inlet pressure P_{in} = 13.1 bar and outlet pressure P_{out} = 7.3 bar ($PR = P_{in}/P_{out}$ = 1.8). The rotor spins at 12,000 rpm ($\frac{1}{2}D\Omega \approx 95$ m/s). The tests produce (through swirl vanes) various inlet pre-swirl velocity ratios ($\alpha = U_{inlet}/R\Omega$) ranging from 0 to 0.5 [5].

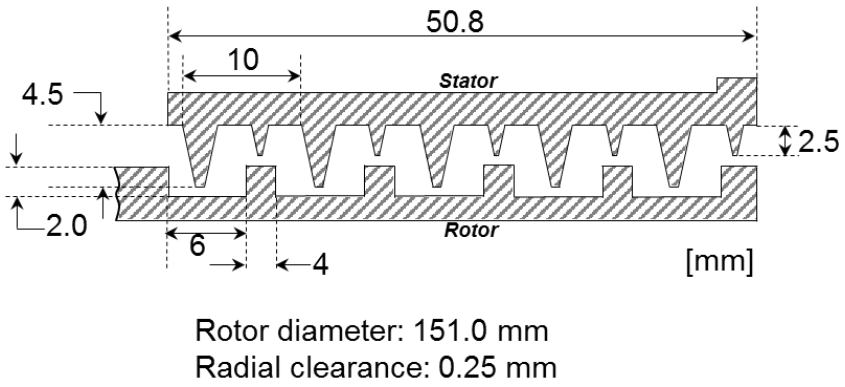

Figure 10. Schematic view of interlocking labyrinth seal in Elrod et al. [5].

Table 4. Interlocking labyrinth seal geometry and operating conditions in Ref. [5]

Geometry	
Rotor diameter, D	151.0 mm
Overall length, L	50.8 mm
Radial clearance, C_r	0.25 mm
TOS tooth pitch, L_{1i}	10 mm
TOS tooth height, B_{1i}	4.5 mm (i=1,3,5,7,9) 2.5 mm (i=2,3,4,8,10)
TOR tooth pitch, L_{2i}	8.0 mm
Tooth height, B_{2i}	2.0 mm
Operating conditions	
Inlet pressure, P_{in}	13.1 bar
Pressure ratio, PR	1.5, 1.8, 2.5
Rotor speed, Ω	12,000 rpm ($\frac{1}{2}D\Omega \approx 95$ m/s)
Pre-swirl ratio, α	BFM: 0, 0.2, 0.3, 0.5 Experiment [5]: 0, 0.2, 0.5

Figure 11 depicts the direct stiffness (K) vs. pre-swirl ratio (α). The pressure ratio ($PR = P_{in}/P_{out}$) ranges from 1.5 to 2.5, and the excitation frequency ω = 38 Hz. Both measurements and the BFM prediction show

[4] Ref. [4] includes no leakage result.

the ILS has a negative direct stiffness, albeit small in magnitude. The BFM prediction reveals the seal K has fairly small changes with respect to the increasing pre-swirl velocity. The BFM predicted K is ~30% of the measured magnitude. When decreasing the pressure ratio (P_{out} increases), the BFM predictions (K) show better agreement with the test data. The BFM predictions of K in Ref. [5] agree well with the test data when the discharge pressure is low (PR = 2.5). However, K predictions in Ref. [5] show an increasing discrepancy with a decrease in pressure ratio (PR). When PR = 1.5, the K predictions in Ref. [5] are approximately 1.7 times larger than the test results.

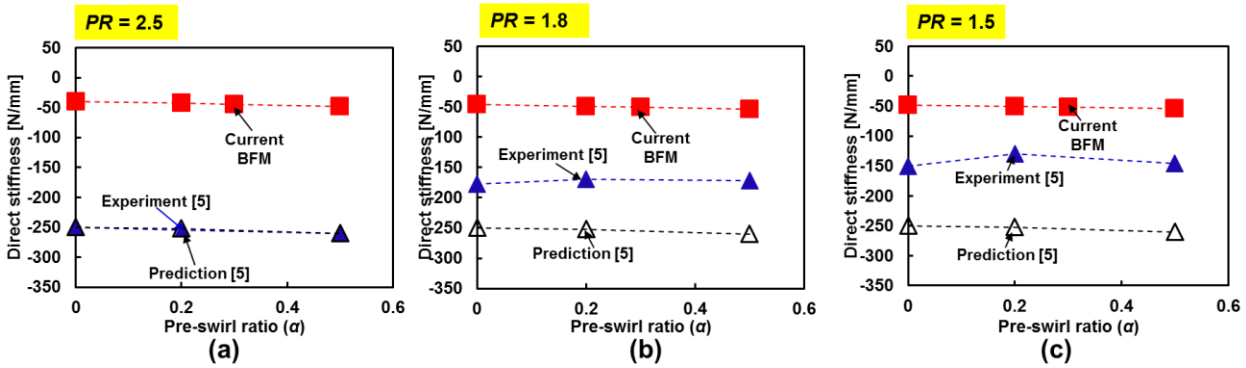

Figure 11. Seal direct stiffness (*K*) vs. inlet pre-swirl ratio (*α*). Interlocking labyrinth seal: (a) *PR* = 2.5, (b) *PR* = 1.8, (c) *PR* = 1.5, Supply pressure P_{in} =13.1 bar, excitation frequency ω = 38 Hz, rotor speed 12,000 rpm (½*D*Ω ≈ 95 m/s).

Figure 12 illustrates the change of cross-coupled stiffness *k* vs. pre-swirl ratio (*α*). Prior research in labyrinth seals (TOR and TOS) evidences *k* is sensitive to the inlet flow pre-swirl ratio. Increasing *α* usually contributes to a higher *k*. From Elrod et al. [5] measurements, *k* is negative when the inlet pre-swirl (*α*) is zero; and *k* increases with an increase in *α*. The test results in Ref. [5] reveal *k* is negative when *α* < 0.5. Predictions of *k* in Ref. [5] show a rather large discrepancy (up to 2.5 times) with the test data. On the other hand, the current BFM predictions agree well with the test *k* when the pre-swirl ratio *α* < 0.2. For *α* > 0.2, the BFM over predicts *k* but still shows better accuracy when compared to the predictions in Ref. [5].

Figure 13 shows the direct damping *C* vs. pre-swirl velocity. When *α* < 0.2, *C* increases with an increase in *α*. For 0.2< *α* < 0.5, *C* decreases with respect to an increase in *α*. As shown in the figure, *C* is over-predicted in Ref. [5]. However, the current BFM predictions match well the test data (within 20%). Both the BFM predictions and the test results evidence the ILS direct damping (*C*) is not as sensitive as *k* to the inlet pre-swirl velocity.

Figure 14 depicts the ILS whirl frequency ratio ($WFR = k/(C\Omega)$) vs. α. The test results reveal the ILS has a negative WFR for $\alpha < 0.5$, while the BFM prediction depicts a cross-over trend at $\alpha \sim 0.3$, after which the WFR becomes positive and keeps increasing with an increase in α. The BFM predicted WFR agrees well (within 18%) with test data for $\alpha < 0.2$, and shows increasing discrepancy with an increase in α. Comparing to the predictions in Ref. [5], the current BFM shows better accuracy in the WFR prediction.

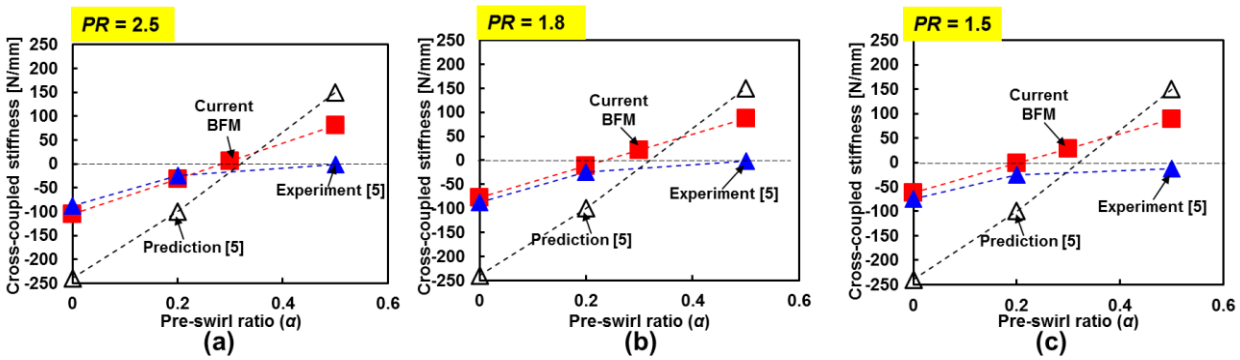

Figure 12. Seal cross-coupled stiffness (*k*) vs. inlet pre-swirl ratio (*α*). Interlocking labyrinth seal: (a) *PR* = 2.5, (b) *PR* = 1.8, (c) *PR* = 1.5, Supply pressure P_{in} =13.1 bar, excitation frequency ω = 38 Hz, rotor speed 12,000 rpm (½*D*Ω ≈ 95 m/s).

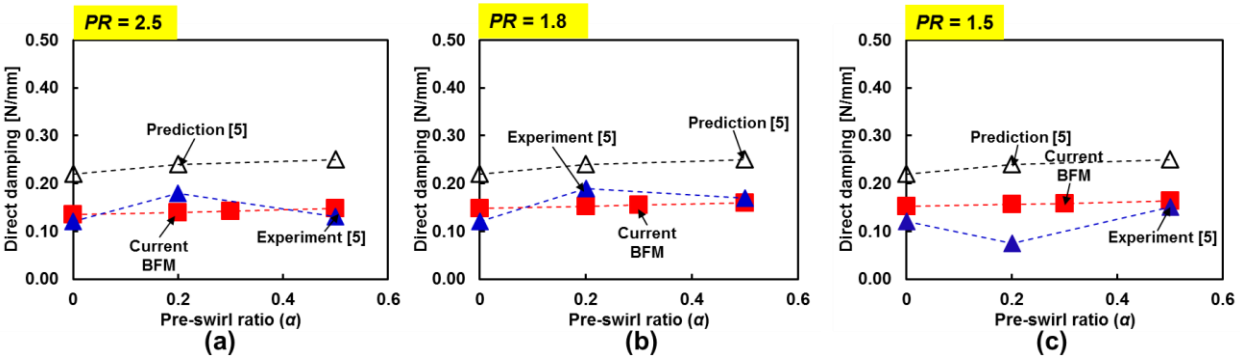

Figure 13. Seal direct damping (*C*) vs. inlet pre-swirl ratio (*α*). Interlocking labyrinth seal: (a) *PR* = 2.5, (b) *PR* = 1.8, (c) *PR* = 1.5, Supply pressure P_{in} =13.1 bar, excitation frequency ω = 38 Hz, rotor speed 12,000 rpm (½*D*Ω ≈ 95 m/s).

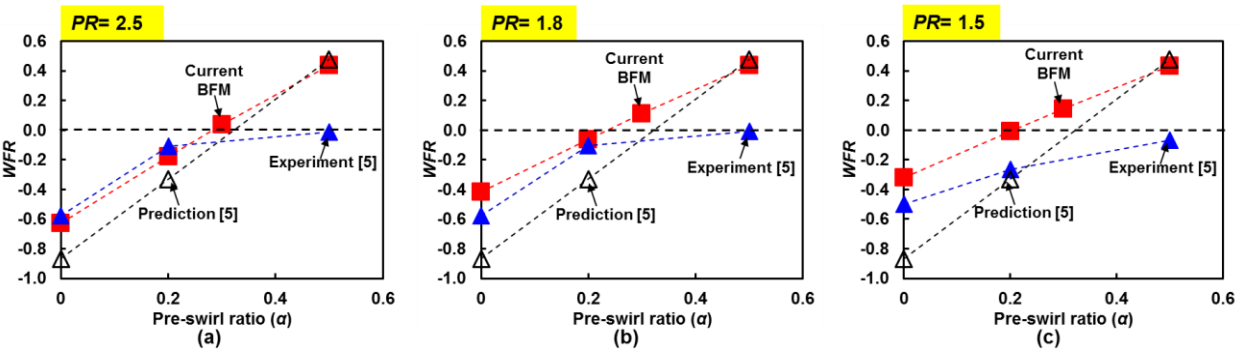

Figure 14. Seal *WFR* vs. inlet pre-swirl ratio (*α*). Interlocking labyrinth seal: (a) *PR* = 2.5, (b) *PR* = 1.8, (c) *PR* = 1.5, Supply pressure P_{in} =13.1 bar, excitation frequency ω = 38 Hz, rotor speed 12,000 rpm (½*D*Ω ≈ 95 m/s).

Example of a Stepped Labyrinth Seal.

Figure 15 shows the schematic view of a stepped LS being tested at TAMU. The ILS design radial clearance C_r = 0.2 mm and L/D = 0.36. However, during the tests, the reported (measured) C_r = 0.08 mm, which is ~1/3 of the design[5] magnitude. The stepped ILS is supplied with air at P_{in} = 10 bar (a) and the discharge pressure P_{out} = 2.8 bar(a), and the rotor speed ranges from 5,000 ~ 10,000 rpm (½$D\Omega \approx$ 39 ~ 78 m/s).

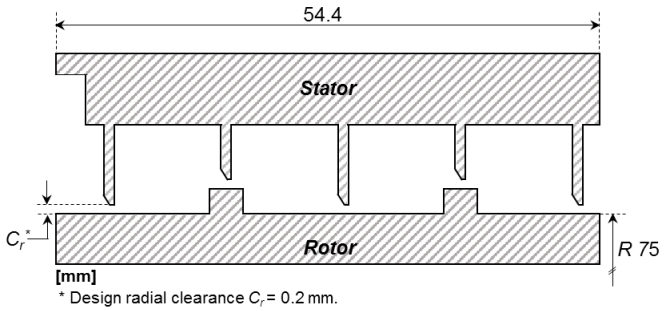

Figure 15. Schematic view of a stepped ILS[6] tested at TAMU. *L/D* = 0.36, nominal C_r = 0.2 mm.

Currently, the rotordynamic force coefficients have not yet been reported, only the mass flow rate ($\dot{m}$) is available. Table 5 lists the stepped ILS mass flow rate ($\dot{m}$), the BFM predictions are in an agreement within 11% with the test data.

Table 5. Mass flow rate of stepped ILS (C_r = 0.08 mm in BFM prediction) recently tested at TAMU.

Rotor Speed		P_{in}	P_{out}	PR	Pre-Swirl Ratio	Mass Flow Rate [g/s]		Difference
[rpm]	[m/s]	[bar]	[bar]	[-]	(α)	Test	BFM	
5,000	39	10	3	3.3	1.02	33.9	36.5	7%
7,500	59	11	3	3.5	0.99	35.6	40.0	11%
10,000	79	11	3	3.5	0.98	36.6	40.0	9%
10,000	79	11	6	2.0	0.94	37.0	33.5	-9%
10,000	79	10	6	1.7	0.93	32.4	29.0	-10%

[5] Reason for this issue is still under investigation.
[6] Detailed geometry not disclosed here due to proprietary restrictions.

6. CONCLUSION

This report details updates to the BFM program (XLLaby©) to predict the leakage and the rotordynamic force coefficients for interlocking labyrinth seals (LS) and stepped LSs. The BFM is based on the governing equations for a one-control volume model derived by Childs and Scharrer [20]. To adapt the geometry of an ILS, dimensionless lengths in circumferential momentum equation are defined as $a_{s_i} = a_{r_i} = (B_i + L_i)/L_i$. The current analysis focuses on the flow conditions leading to choked flow and presents a simple equation to estimate its onset.

The zeroth order solution gives the seal leakage as well as the cavity pressure and circumferential velocity distributions. The predicted leakage, cavity pressures, and the circumferential velocity are validated against predictions from a 2D CFD analysis. A perturbation analysis renders the seal rotordynamic force coefficients, frequency dependent.

Current BFM predictions for force coefficients are compared against test data in Ref. [5] and show good agreement for cross-coupled stiffness and direct damping. The predictions reveal the interlocking labyrinth seal has a negative direct stiffness (*K*) albeit small in magnitude. Increasing the pre-swirl ratio (α) has a fairly small impact on *K*. The predicted cross-stiffness *k* matches well with the test data when $\alpha < 0.2$. For $0.2 < \alpha < 0.5$, the predicted *k* is away from the test result. On the other hand, the BFM accurately predicts the direct damping *C* coefficient.

In sum, the current BFM predicts more accurately the leakage and force coefficients of an ILS, as compared to prior predictions in Ref. [5]. However, the poor prediction of direct stiffness *K* merits further investigation.

NOMENCLATURE

A	Cross-sectional area of a cavity [m^2]
b_1	$b_1 = 1 - \left(\frac{\gamma+1}{2}\right)^{-\frac{2\gamma}{\gamma-1}}$ (=0.729, for air)
B	Height of the labyrinth seal strip [mm]
C, c	Direct and cross-coupled damping coefficients [N·s/m]
C_r	Seal radial clearance [mm]
C_s	Exit discharge coefficient
D	Rotor diameter [mm]
D_h	Hydraulic diameter [mm]
E	Rotor dynamic eccentricity [mm]
f	Friction factor, $f_{r,s} = n_{r,s}Re^{m_{r,s}}$
F_X, F_Y	Components of seal reaction force [N]
H	Local clearance function [mm]
K, k	Direct and cross-coupled stiffness coefficients [N/m]
L	Seal length [mm]
L_i	Pitch length [mm]
L_t	Tooth width [mm]
$\bar{\dot{m}}$	Mass flow rate per circumference length [g/(ms)]
$\dot{m}$	Mass flow rate [g/s]
n_r, m_r, n_s, m_s	Empirical coefficients for *Blasius* friction factor
NT	Number of tooth
NC	Number of cavity, NT-1
P_i	i^{th} cavity pressure [Pa]
P_{in}	Supply pressure [Pa]
P_{out}	Discharge pressure [Pa]
PR	Pressure ratio, $PR = P_{in}/P_{out}$
r_c	Critical pressure ratio
Re	Reynolds number, $\mathrm{Re}_{r,s} = U_{r,s}D_h/v$
R_g	Gas constant
R_s	Rotor radius [mm]
t	Time [s]
T	Temperature [K]
U	Bulk-flow circumferential velocity in cavity [m/s]
W	Bulk-flow axial velocity [m/s]
WFR	Whirl frequency ratio, $WFR = k/(C\Omega)$
X, Y	Rotor displacements [m]
Z_g	Compressibility factor
α	Inlet pre-swirl ratio, $\alpha = U_{inlet}/R\Omega$
β	$\beta_i = \left(\frac{P_{i-1}}{P_i}\right)^{\frac{\gamma-1}{\gamma}} - 1$
γ	Specific heat ratio
θ	Circumferential direction
λ	$\lambda = 1 - \left(1 + 16.6C_r / L_i\right)^{-2}$
μ_{1i}	Kinetic energy carry-over coefficient
μ_{2i}	Flow discharge coefficient
v	Kinematic viscosity $v = \mu/\rho$ [m^2/s]

ξ	Entrance loss coefficient
ρ	Density, $P/(Z_g R_g T)$ [kg/m^3]
τ	Shear stress [N]
ω	Excitation frequency [rad/s]
Ω	Rotor speed [rad/s]

Subscripts

0	Zeroth-order component
1	First-order component
i	i^{th} chamber value
r	Rotor surface
s	Stator surface

Abbreviations

BFM	Bulk-flow model
CFD	Computational fluid dynamics
CV	Control volume
ILS	Interlocking labyrinth seal
LS	Labyrinth seal
TOR	Tooth on rotor labyrinth seal
TOS	Tooth on stator labyrinth seal

REFERENCES

[1] Ek, M., 1978, "Solution of the Subsynchronous Whirl Problem in the High-Pressure Hydrogen Turbomachinery of the Space Shuttle Main Engine," 14th Joint Propulsion Conference, Las Vegas, July 25-27, pp. 100201-100226.

[2] Childs, D. W., 1993, *Turbomachinery Rotordynamics: Phenomena, Modeling, and Analysis*, Chap.5, "Rotordynamic Models for Annular Gas Seals", John Wiley & Sons.

[3] Kuwamura, Y., Matsumoto, K., Uehara, H., Ooyama, H., Tanaka, Y., and Nishimoto, S., 2013, "Development of New High-Performance Labyrinth Seal Using Aerodynamic Approach," ASME Paper GT2013-94106.

[4] Gao, R., and Kirk, G., 2013, "CFD Study on Stepped and Drum Balance Labyrinth Seal," Tribol T, **56**(4), pp. 663-671.

[5] Elrod, D. A., Pelletti, J. M., and Childs, D. W., 1995, "Theory versus Experiment for the Rotordynamic Coefficients of an Interlocking Labyrinth Gas Seal," ASME Paper 95-GT-432.

[6] Benckert, H., and Wachter, J., 1978, "Studies on Vibrations Stimulated by Lateral Forces in Sealing Gaps," AGARD Seal Technology in Gas Turbine Engineering, UK.

[7] Leong, Y., and Brown, R., 1984, "Experimental Investigation of Lateral Forces Induced by Flow through Model Labyrinth Glands," Proceedings of a Workshop on Rotordynamic Instability Problems in High-Performance Turbomachinery, Texas A&M University, College Station, TX, pp. 187-210.

[8] Childs, D. W., and Scharrer, J. K., 1986, "Experimental Rotordynamic Coefficient Results for Teeth-on-Rotor and Teeth-on-Stator Labyrinth Gas Seals," ASME J Eng Gas Turb Power, **108**(4), pp. 599-604.

[9] Thieleke, G., and Stetter, H., 1990, "Experimental Investigations of Exciting Forces Caused by Flow in Labyrinth Seals," Proceeding of a Workshop on Rotordynamic Instability Problems in High-Performance Turbomachinery, Texas A&M University, College Station, TX, pp. 109-134.

[10] Childs, D. W., Elrod, D. A., and Hale, K., 1988, "Rotordynamic Coefficient and Leakage Test Results for Interlock and Tooth-on-Stator Labyrinth Seals," ASME Paper 88-GT-87.

[11] Picardo, A., and Childs, D. W., 2005, "Rotordynamic Coefficients for a Tooth-on-Stator Labyrinth Seal at 70 Bar Supply Pressures: Measurements versus Theory and Comparisons to a Hole-Pattern Stator Seal," ASME J Eng Gas Turb Power, **127**(4), pp. 843-855.

[12] Wagner, N. G., Steff, K., Gausmann, R., and Schmidt, M., 2009, "Investigations on the Dynamic Coefficients of Impeller Eye Labyrinth Seals," Proceedings of the 38th Turbomachinery Symposium, Houston, TX, September 14-17.

[13] Ertas, B. H., Delgado, A., and Vannini, G., 2012, "Rotordynamic Force Coefficients for Three Types of Annular Gas Seals with Inlet Preswirl and High Differential Pressure Ratio," ASME J Eng Gas Turb Power, **134**(4), pp. 042503-042512.

[14] Vannini, G., Cioncolini, S., Del Vescovo, G., & Rovini, M. , 2014, "Labyrinth Seal and Pocket Damper Seal High Pressure Rotordynamic Test Data," ASME J Eng Gas Turb Power, **136**(2), pp. 022501-022509.

[15] Alford, J. S., 1965, "Protecting Turbomachinery from Self-Excited Rotor Whirl," ASME J Eng P, **87**(4), pp. 333-343.

[16] Murphy, B., and Vance, J., 1980, "Labyrinth Seal Effects on Rotor Whirl Instability," Proceedings of the 2nd International Conference on Vibrations in Rotating Machinery, Cambridge, England, September 1-4.

[17] Kostynk, A., 1972, "Theoretical Analysis of the Aerodynamic Forces in the Labyrinth Glands of Turbomaehines," Therm Eng, **19**(11), pp. 29-33.

[18] Iwatsubo, T., 1980, "Evaluation of Instability Forces of Labyrinth Seals in Turbines or Compressors," Proceedings of a Workshop on Rotordynamic Instability Problems in High-Performance Turbomachinery, Texas A&M University, College Station, TX, pp. 139-167.

[19] Iwatsubo, T., Motooka, N., and Kawai, R., 1982, "Flow Induced Force of Labyrinth Seal," Proceedings of a Workshop on Rotordynamic Instability Problems in High-Performance Turbomachinery, Texas A&M University, College Station, TX, pp. 205-222.
[20] Childs, D. W., and Scharrer, J. K., 1986, "An Iwatsubo-Based Solution for Labyrinth Seals: Comparison to Experimental Results," ASME J Eng Gas Turb Power, **108**(2), pp. 325-331.
[21] Scharrer, J., 1988, "Theory versus Experiment for the Rotordynamic Coefficients of Labyrinth Gas Seals: Part I-A Two Control Volume Model," ASME J Vib Acoust, **110**(3), pp. 270-280.
[22] Childs, D., and Scharrer, J., 1988, "Theory versus Experiment for the Rotordynamic Coefficients of Labyrinth Gas Seals: Part II-A Comparison to Experiment," ASME J Vib Acoust, **110**, pp. 281-287.
[23] Moore, J. J., 2003, "Three-Dimensional CFD Rotordynamic Analysis of Gas Labyrinth Seals," ASME J Vib Acoust, **125**(4), pp. 427-433.
[24] Li, Z., Li, J., and Yan, X., 2013, "Multiple Frequencies Elliptical Whirling Orbit Model and Transient RANS Solution Approach to Rotordynamic Coefficients of Annual Gas Seals Prediction," ASME J Vib Acoust, **135**(3), pp. 031005-031014.
[25] Migliorini, P. J., Untaroiu, A., Wood, H. G., and Allaire, P. E., 2012, "A Computational Fluid Dynamics/Bulk-Flow Hybrid Method for Determining Rotordynamic Coefficients of Annular Gas Seals," ASME J Tribol, **134**(2), pp. 0222021-0222029.
[26] Migliorini, P. J., Untaroiu, A., Witt, W. C., Morgan, N. R., and Wood, H. G., 2014, "Hybrid Analysis of Gas Annular Seals with Energy Equation," ASME J Tribol, **136**(3), pp. 0317041-0317049.
[27] Childs, D. W., and Wade, J., 2004, "Rotordynamic Coefficient and Leakage Characteristics for Hole-Pattern-Stator Annular Gas Seals-Measurements versus Predictions," ASME J Tribol, **126**(2), pp. 326-333.
[28] San Andres, L. A., 1991, "Analysis of Variable Fluid Properties, Turbulent Annular Seals," ASME J Tribol, **113**(4), pp. 694-702.
[29] Yèucel, U., 1996, "Leakage and Swirl Velocities in Labyrinth Seals," M.S. Thesis, Department of Applied Mathematics, Lehigh University.
[30] Gurevich, M. I., 1966, *The Theory of Jets in an Ideal Fluid*, Pergamon Press, Oxford, pp. 235-256.

APPENDIX

Introduction to (2017) Modified XLLABY© GUI

The modified XLLABY© shares a similar GUI with the original XLLABY© program.

Figure 16 depicts the Excel based graphical user interface of the modified program. In the figure, **section A** contains the seal dimensions, fluid (compressible) properties input and the outputs. As with the original XLLABY©, the modified program allows users to switch between SI units and British units, however, one should notice that switch the units will only change the units not a conversion. XLLABY© provides two leakage models, namely: Neumann Model and Gamal Model. As discussed in the report, the program modification is based on the "Neumann Model". Analysis for ILS is not supported when "Gamal Model" is selected.

The modified XLLABY© has the capability to predict the leakage and rotordynamic coefficients of TOR, TOS and ILS (including stepped) labyrinth seals. The option of "Tooth Location" allows *User* to switch the seal type, where "Rotor" stands for TOR, "Stator" for TOS, and "Interlock" for ILS (for stepped LS, use "Interlock").

The *User* defines seal dimensions in the seal properties part in **Section A**, whereas **Section B** includes the schematic view of TOR, TOS and ILS labyrinth seals. Empirical coefficients for the rotor/stator friction model are provided as default value. However, the *User* may also enter those coefficients based on available experimental data.

In **section C** the *User* sets the gas properties and operating conditions (supply pressure P_{in}, sump pressure P_{out}, and inlet pre-swirl ratio λ, and whirl speed ω). The "Parameters" part gives out some frequently used ratios based on the *User* inputs.

Section D includes the outputs (rotordynamic force coefficients (K, k, C, c), rotor surface Mach number, leakage and *WFR*) with respect to the rotor speed (*User* input). After inputting all the parameters.

User clicks "Run" to obtain the predictions. One may notice that the modified XLLABY© (neither does the original code) does not output added mass coefficients (M, m).

Click the labels (*XLLaby*, *Curve Fit*, *K Chart*, and *C Chart*) on the bottom, *Users* could switch to the curve fit process. *User* presses the "Update Curve Fits" button, the curve fit process will be automatically conducted as shown in

Figure 17.

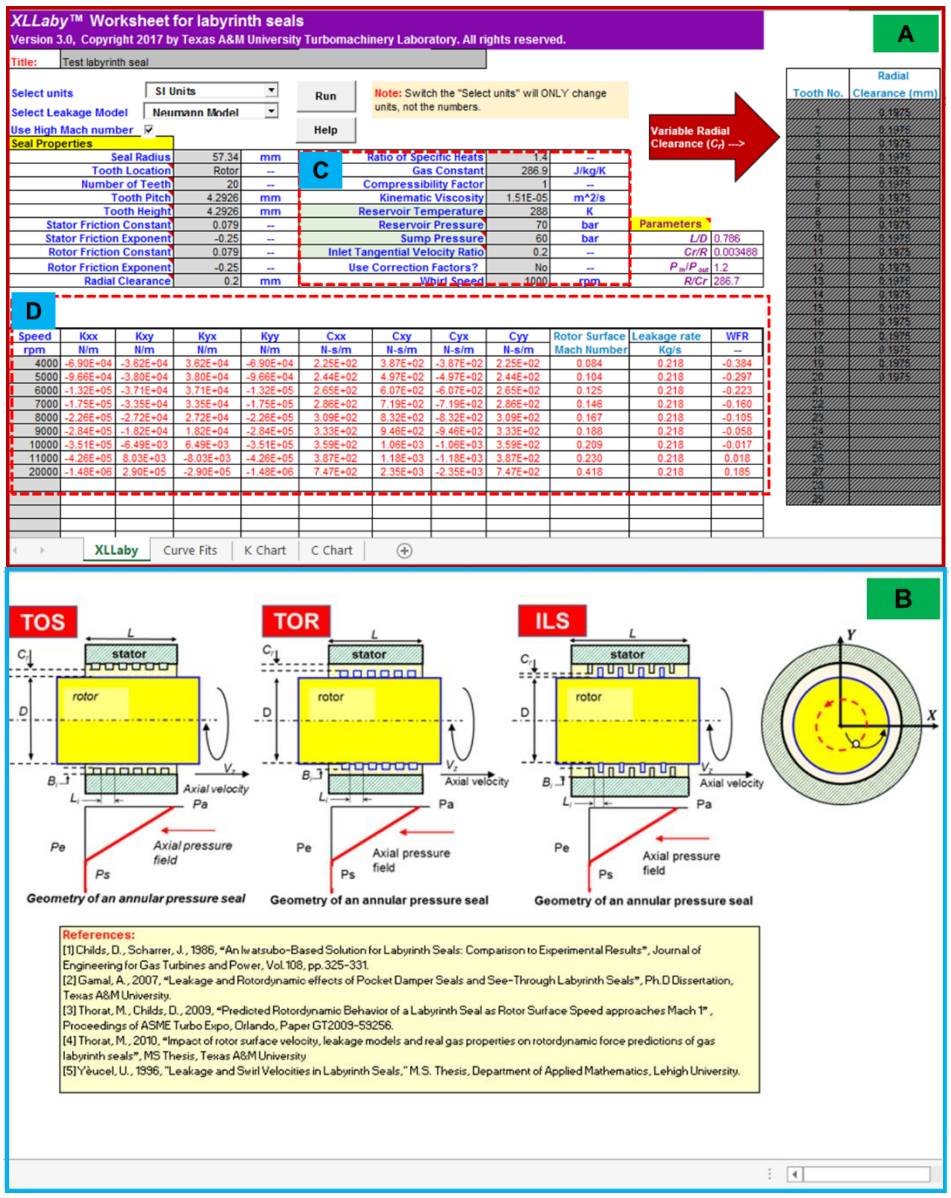

Figure 16. Modified XLLABY© GUI

Curve Fits

Order of Fit	5	(1=line, 2=parabola, etc.)
First Power of Fit	0	(normally 0, sometimes -1)

Update Curve Fits

Coef.	Kxx	Kxy	Kyx	Kyy	Cxx	Cxy	Cyx	Cyy
0	-35244.89978	4006.803223	-4006.803223	-35244.89978	149.65113	-32.80951095	32.80951095	149.65113
1	6.896383047	-17.7310475	17.7310475	6.896383047	0.01967074	0.100184674	-0.100184674	0.01967074
2	-0.003841758	0.002231138	-0.002231138	-0.003841758	-5.5292E-07	1.62399E-06	-1.62399E-06	-5.5292E-07
3	4.49247E-09	-9.35044E-08	9.35044E-08	4.49247E-09	9.64707E-11	-1.26539E-10	1.26539E-10	9.64707E-11
4	-4.98458E-13	4.341E-12	-4.341E-12	-4.98458E-13	-3.55677E-15	6.78179E-15	-6.78179E-15	-3.55677E-15
5	-1.59186E-18	-6.21133E-17	6.21133E-17	-1.59186E-18	6.94317E-20	-1.08708E-19	1.08708E-19	6.94317E-20

Speed fit	Kxx fit	Kxy fit	Kyx fit	Kyy fit	Cxx fit	Cxy fit	Cyx fit	Cyy fit
4000.0	-68969.2	-36155.77193	36155.77193	-68969.2	224.822055	387.4394054	-387.4394054	224.822055
5777.8	-123346.7	-37555.04159	37555.04159	-123346.7	259.93675	582.6997029	-582.6997029	259.93675
7555.6	-202177.0	-30306.39695	30306.39695	-202177.0	298.4385278	781.6947417	-781.6947417	298.4385278
9333.3	-305781.1	-14606.75169	14606.75169	-305781.1	341.4409155	984.597619	-984.597619	341.4409155
11111.1	-434613.9	9825.120013	-9825.120013	-434613.9	389.8335833	1192.222714	-1192.222714	389.8335833
12888.9	-589267.4	43616.22455	-43616.22455	-589267.4	444.4302975	1405.794037	-1405.794037	444.4302975
14666.7	-770474.6	87606.99	-87606.99	-770474.6	506.1168756	1626.713582	-1626.713582	506.1168756
16444.4	-979112.3	142718.9072	-142718.9072	-979112.3	575.9991395	1856.329674	-1856.329674	575.9991395
18222.2	-1216205.0	209822.1709	-209822.1709	-1216205.0	655.5508699	2095.705324	-2095.705324	655.5508699
20000.0	-1482927.9	289603.3207	-289603.3207	-1482927.9	746.7617598	2345.386572	-2345.386572	746.7617598

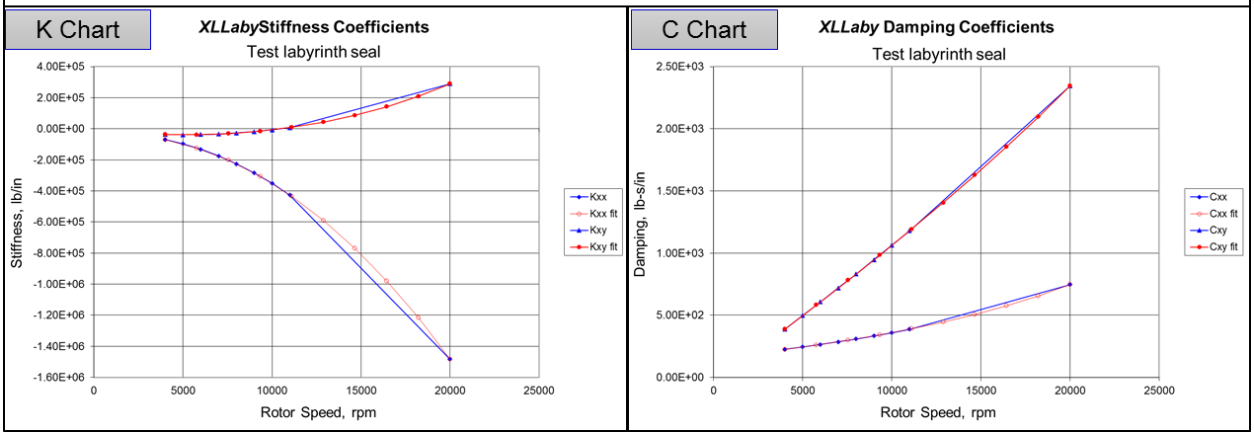

Figure 17. Modified XLLABY© GUI (Cont.)